

# Biocompatible Magnetic Micro- and Nanodevices: Fabrication of FePt Nanopropellers and Cell Transfection

Vincent Mauricio Kadiri, Claudio Bussi, Andrew W. Holle, Kwanghyo Son, Hyunah Kwon, Gisela Schütz, Maximiliano G. Gutierrez,\* and Peer Fischer\*

The application of nanoparticles for drug or gene delivery promises benefits in the form of single-cell-specific therapeutic and diagnostic capabilities. Many methods of cell transfection rely on unspecific means to increase the transport of genetic material into cells. Targeted transport is in principle possible with magnetically propelled micromotors, which allow responsive nanoscale actuation and delivery. However, many commonly used magnetic materials (e.g., Ni and Co) are not biocompatible, possess weak magnetic remanence ( $\text{Fe}_3\text{O}_4$ ), or cannot be implemented in nanofabrication schemes (NdFeB). Here, it is demonstrated that co-depositing iron (Fe) and platinum (Pt) followed by one single annealing step, without the need for solution processing, yields ferromagnetic FePt nanomotors that are noncytotoxic, biocompatible, and possess a remanence and magnetization that rival those of permanent NdFeB micromagnets. Active cell targeting and magnetic transfection of lung carcinoma cells are demonstrated using gradient-free rotating millitesla fields to drive the FePt nanopropellers. The carcinoma cells express enhanced green fluorescent protein after internalization and cell viability is unaffected by the presence of the FePt nanopropellers. The results establish FePt, prepared in the  $\text{L1}_0$  phase, as a promising magnetic material for biomedical applications with superior magnetic performance, especially for micro- and nanodevices.

Nanoscope and microscopic probes aimed at providing biosensory feedback, transfecting cells, or killing tumors are a major effort in the field of nanobiomedicine.<sup>[1,2]</sup> Magnetic particles are considered promising, as they offer diagnostic functions and can provide in vivo imaging contrast in nuclear magnetic resonance imaging (MRI), computer tomography (CT), or magnetic particle imaging (MPI).<sup>[3–6]</sup> Magnetic  $\gamma\text{-Fe}_2\text{O}_3$  or  $\text{Fe}_3\text{O}_4$  particles can also be used for hyperthermia treatment (magnetothermal destruction) of tumor tissue. Yet many authors have concluded that active targeting, i.e., the directed chemical or physical taxis toward a target site, coupled with the capability for gene delivery is a crucial necessity for these probes. In recent years, many types of micro- and nanomotors, most prominently Janus particles actuated by various chemical or physical stimuli (hydrogen peroxide, glucose, light, heat, electric fields, etc.) are being investigated to address this challenge.<sup>[7–11]</sup>


Magnetic-particle-based systems are particularly promising as they can be manipulated via magnetic fields for targeted delivery applications. While homogenous and static fields are used for imaging, the directed motion of nanostructures is typically achieved with strong magnetic field gradients. However, it is challenging to achieve large gradients over sizeable distances, as would be required for applications inside the body. It has, therefore, been demonstrated to be more practical to use weak rotating homogenous magnetic fields to direct screw-like nanomotors.<sup>[9,12–17]</sup> Magnetically propelled helical nanomotors (MPNs), unlike superparamagnetic iron oxide nanoparticles (SPIONs), are typically actuated by 5–10 mT rotating fields in a variety of media. We have recently demonstrated the penetration of biological media such as the gastric mucus and actuation within the vitreous of the eye with magnetically propelled helical nanomotors or “nanopropellers.”<sup>[18,19]</sup> MPNs have also been moved through blood,<sup>[20]</sup> and larger zinc- or magnesium-based Janus micromotors have been manipulated in the stomach and intestine.<sup>[21–24]</sup> It has also been shown that if the dimensions of the nanopropellers are sufficiently small, they can move unhindered through the biopolymeric network found in tissues.<sup>[25]</sup> These small helical nanopropellers can be grown using a physical vapor deposition

V. M. Kadiri, Dr. K. Son, Dr. H. Kwon, Prof. G. Schütz, Prof. P. Fischer  
Max Planck Institute for Intelligent Systems  
Heisenbergstr. 3, Stuttgart 70569, Germany  
E-mail: fischer@is.mpg.de

V. M. Kadiri, Prof. P. Fischer  
Institute of Physical Chemistry  
University of Stuttgart  
Pfaffenwaldring 55, Stuttgart 70569, Germany

Dr. C. Bussi, Dr. M. G. Gutierrez  
Francis Crick Institute  
1 Midland Rd, London NW1 1AT, UK  
E-mail: max.g@crick.ac.uk

Dr. A. W. Holle  
Max Planck Institute for Medical Research  
Jahnstraße 29, Heidelberg 69120, Germany

 The ORCID identification number(s) for the author(s) of this article can be found under <https://doi.org/10.1002/adma.202001114>.

© 2020 The Authors. Published by WILEY-VCH Verlag GmbH & Co. KGaA, Weinheim. This is an open access article under the terms of the Creative Commons Attribution License, which permits use, distribution and reproduction in any medium, provided the original work is properly cited.

DOI: 10.1002/adma.202001114

method from a range of materials;<sup>[25]</sup> i.e., unary or binary ferromagnetic materials can be incorporated during the growth. The magnetic sections can then be magnetized perpendicularly to the long axis of the helix. The magnetic moment will align along the field lines of an applied magnetic field. Rotation of the magnetic field thus creates a torque on the helical structure. Rotation–translation coupling leads to propulsion in synchrony with the magnetic field up to a “step-out” frequency where the applied torque is no longer able to counter the rotational drag.<sup>[26]</sup>

One commonly cited application of micromotors and nanomotors is their use to deliver DNA or other pharmacocactive cargo.<sup>[11]</sup> Gene and drug delivery is in principle possible with MPNs,<sup>[27–29]</sup> and Pal et al. have recently even shown the maneuverability of magnetic nanopropellers inside live cells.<sup>[30,31]</sup> Yet these MPNs all either utilize directly deposited magnetic elements such as soft-magnetic Fe or Ni fabricated using physical growth methods or superparamagnetic Fe<sub>3</sub>O<sub>4</sub> as materials for the magnetic section. However, many magnetic materials are unsuitable for biological applications: Co and Ni are toxic<sup>[32–38]</sup> and Fe is relatively unstable toward corrosion and oxidation.<sup>[39–41]</sup> Direct deposition of iron oxides is difficult with electron beam and thermal evaporation methods, and vacuum growth of FeO<sub>x</sub> typically requires oxygen treatment and careful procedures to obtain the correct stoichiometry and magnetic phase.<sup>[42,43]</sup> It is in principle also possible to subject nonmagnetic helical microstructures to post-treatment to obtain biocompatible magnetic coatings either by forming a zinc ferrite (Zn<sub>x</sub>Fe<sub>3–x</sub>O<sub>4</sub>) layer<sup>[44]</sup> or by coupling magnetic nanoparticles to the structure.<sup>[45]</sup> However, both require solution processing and multiple fabrication steps. Alternately, one can include magnetic nanoparticles in a photocrosslinkable polymer,<sup>[46,47]</sup> but this is a slower serial fabrication method and the inclusion of magnetic nanoparticles leads to weaker moments in turn requiring higher fields for actuation. It is therefore desirable to develop a system that is at the same time relatively easy to manufacture, biocompatible and a hard-magnet for targeted magnetic motors and gene delivery.

Particularly promising as a hard-magnetic biocompatible material is the face-centered tetragonal (fct) L1<sub>0</sub> phase of FePt, which has been shown to be nonimmunogenic, noncytotoxic, and highly biocompatible while offering strong magnetic remanence.<sup>[4]</sup> FePt attracted much interest since it is a chemically stable rare-earth-free permanent magnet with high magnetocrystalline anisotropy. Nanosized FePt exhibits high saturation and remanent magnetization, large coercivity, and large energy products. Son et al. recently discussed the merits of the material for magnetic micro- and nanodevices in depth.<sup>[48]</sup>

Here, we co-deposit Fe and Pt, excellent materials for e-beam deposition, onto SiO<sub>2</sub> and show that in one single annealing step, without the need for solution processing, we obtain nanopropellers for cell transfection that contain ferromagnetic L1<sub>0</sub> FePt, which is biocompatible and shows very high magnetic remanence rivaling NdFeB micromagnets.

We employ a parallel physical vapor deposition method, termed glancing angle deposition<sup>[49]</sup> (GLAD), for the growth of FePt-containing nanopropellers imaged in Figure S1 in the Supporting Information. Briefly, a substrate is first patterned with 500 nm silica beads. The silica beads serve as a seed layer during the vacuum deposition at an angle of 85° while the substrate is rotated to form 1.5 μm silica helices.<sup>[12]</sup>

A small ≈350 nm section is then grown onto the helices via the co-deposition of Fe and Pt to later form the magnetic layer for propulsion. The general scheme depicting fabrication, surface functionalization, and propulsion of helical nanopropellers can be seen in Figure 1.

The molar ratio of Fe to Pt is confirmed by inductively coupled plasma (ICP) elemental analysis to be 1:1 (Figure S2, Supporting Information). Grazing angle X-ray diffraction (XRD) characterization of the wafer with Cu Kα radiation is performed and yields the reflex pattern pictured in Figure 2a, which indicates the presence of a face-centered cubic (fcc) phase or an amorphous phase of FePt. To obtain the fct L1<sub>0</sub> phase of FePt, which is the interesting phase for magnetic applications, an annealing procedure is adapted according to previous studies.<sup>[50]</sup> The transition to fct L1<sub>0</sub> FePt could be clearly observed in the XRD patterns after annealing steps at 300, 680, and 800 °C, as shown in Figure 2a. Peaks for the fct L1<sub>0</sub> phase of FePt are assigned according to two calculated XRD reference patterns (Mercury 4.2 and recipOgraph) and also match the relative intensities of previous studies.<sup>[51–54]</sup> Samples annealed at 680 and 800 °C exhibit the characteristic peaks at  $2\theta = 42^\circ$ ,  $48^\circ$ , and  $82^\circ$ , corresponding to the (101), (110) and (211) planes, respectively,<sup>[54,55]</sup> while as-deposited samples as well as those annealed at 300 °C show only the characteristic (101) and (110) peaks indicating a nearly amorphous or fcc phase of FePt. These results indicate that after annealing at 680 °C the magnetic FePt section in the nanopropellers possess the fct L1<sub>0</sub> crystal phase.

Magnetic characterization of the samples via SQUID magnetometry (Figure 2b,c) confirms that the desired phase is obtained after annealing at 680 °C, when the FePt becomes a hard-magnet, in agreement with earlier studies.<sup>[52,55]</sup> The critical domain size for L1<sub>0</sub> FePt is around 50 nm.<sup>[56]</sup> Since the FePt magnetic section for nanomotors are one order of magnitude larger than the critical domain size, FePt is assumed to be present as multiple magnetic domains. The interaction between the domains leads to a slightly lower hard magnetic performance than what may theoretically be possible. After magnetizing the magnetic sections along their easy (longitudinal) axis in a 5 T field, which corresponds with the in-plane magnetization for a wafer of perpendicularly grown helices, they exhibited magnetic moments of  $2.42 \times 10^{-12}$  emu per propeller. Based on the volume of the magnetic domain as pictured, e.g., in Figure S1c in the Supporting Information this corresponds to a strong remanent magnetization of  $\approx 333$  emu cm<sup>-3</sup>. The magnetization of bulk NdFeB is  $\approx 1270$  emu cm<sup>-3</sup>,<sup>[57]</sup> while experimentally measured microstructured NdFeB showed  $\approx 400$  emu cm<sup>-3</sup> magnetic moments with another literature value suggesting 700 emu cm<sup>-3</sup>.<sup>[58]</sup> Critically however, NdFeB as a material is neither chemically inert,<sup>[59]</sup> nor can it be nanostructured or incorporated in nanodevices during growth. In contrast, L1<sub>0</sub> FePt fulfills these requirements in addition to being rare-earth free, making it an attractive substitute material for the construction of high magnetic remanence micro-sized hard magnetic materials and devices.

FePt also presents various qualitative and quantitative benefits when compared to other possible magnetic materials. Cobalt, nickel, iron, iron oxides, and zinc ferrite have at different times all been used in the fabrication of nanopropellers. However, zinc ferrite while biocompatible, requires an

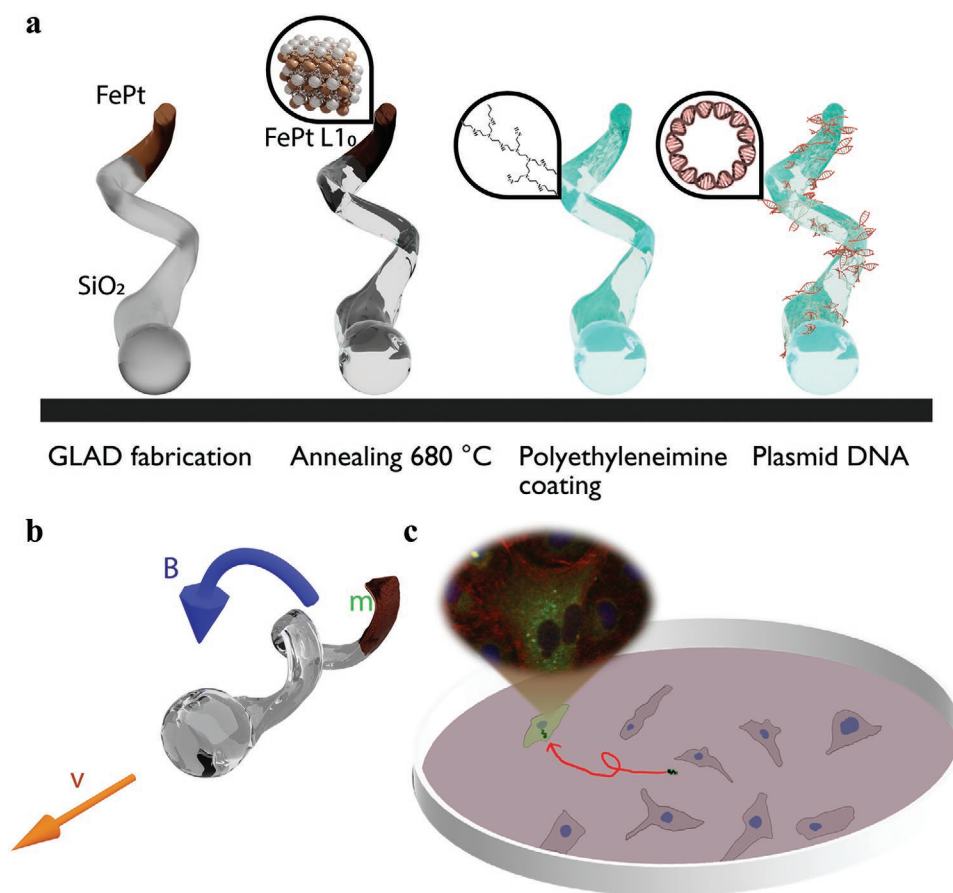


**Figure 1.** Illustration of  $L_{10}$  FePt nanomotor fabrication, working principle, and application. a) Magnetically propelled helical nanomotors (nanopropellers) fabricated by glancing angle deposition are annealed at 680 °C and functionalized with polyethyleneimine (PEI) and plasmid DNA. b) Nanopropellers exhibit high magnetic moments  $m$  that enable movement via small external rotating magnetic fields  $B$ . c) Nanopropellers can navigate through cell media, transfect cells, and deliver genetic material.

additional chemical solution-processing step post PVD (GLAD) deposition.<sup>[44]</sup> Cobalt and nickel are both known to be toxic,<sup>[32]</sup> leaving iron and iron oxide as possible contenders for our simplified fabrication scheme. However, depositing the correct phase of iron oxide would require careful postprocessing.<sup>[43]</sup> Last, iron metal has the tendency to oxidize into  $\text{FeO}_x$ , which generally exhibits a significantly lower magnetic remanence compared to FePt. FePt is chemically inert, hard-magnetic, and biocompatible,<sup>[3]</sup> and thus possesses superior properties compared to all other magnetic materials, when it comes to the use of magnetic micromotors and nanorobotics systems for biomedical applications.

A difficulty in comparing magnetic materials is that there is no unified convention for reporting the magnetic characteristics of magnetic microdevices. We appreciate that this is a difficulty that needs to be addressed to permit the easy comparison between magnetic materials and devices. To enable a direct comparison between magnetic materials and the performance of magnetic micromotors, we choose to report and compare the magnetic remanence, coercive field  $H_C$  and saturation magnetization  $M_S$  for FePt-, Fe-, and Ni-based nanopropellers that have all been fabricated by the same GLAD system and method<sup>[18,19]</sup> (Table S1, Supporting Information). We report the volume remanence magnetization in  $\text{emu cm}^{-3}$  as this

measure allows for a comparison with literature values of bulk magnetic materials. The volume remanence magnetization can be obtained from SQUID data with a careful calculation of the volume based on transmission electron microscopy (TEM) and scanning electron microscopy (SEM) images (which many researchers already incorporate into their characterization). While we also report the  $\text{emu nanopropeller}^{-1}$  and  $\text{emu mm}^{-2}$  wafer, we note that these, as well as the  $\text{emu g}^{-1}$  can be misleading since propeller sizes, the amount of particles per wafer, and magnetic material incorporated can vary significantly for magnetic microdevices.

Nevertheless, we consistently find that FePt has an 8-fold higher remanent magnetization compared to Fe nanopropellers ( $40 \text{ emu cm}^{-3}$ ) and a 30-fold higher remanent magnetization compared to Ni-based ( $11 \text{ emu cm}^{-3}$ ) structures grown using the same fabrication method. Additionally, FePt possesses a lower tendency to oxidize and a higher coercivity (Figure 2d,e; Figure S3 and Table S1, Supporting Information). FePt thus represents a major improvement in the magnetic properties of helical nanopropellers.<sup>[18]</sup> We expect that the optimization of fabrication and post-treatment steps will lead to further increases in magnetic performance.

Since the samples annealed at 680 °C show the highest in-plane remanence, these are selected for nanopropeller

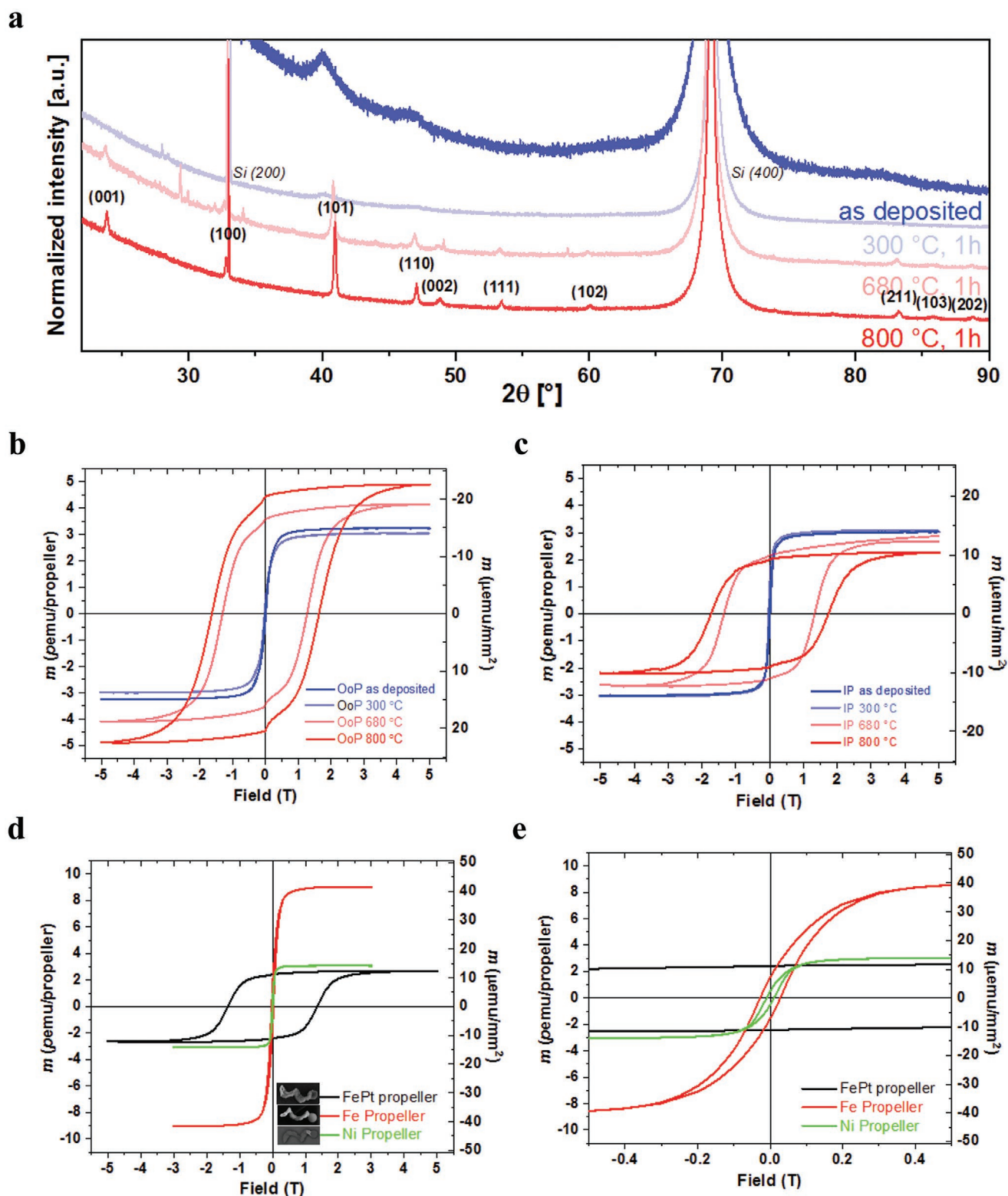


**Figure 2.** Characterization of as-deposited (dark blue) propellers and after annealing steps at 300 (light blue), 680 (light red), and 800 °C for 1 h (red). a) Characteristics of crystalline,  $L1_0$  peaks become more pronounced in the XRD diffractogram after annealing the nanomotors at 680 or 800 °C. b,c) Magnetic characterization: The magnetic hysteresis loops show saturation magnetization ( $M_s$ ) and coercive field ( $H_c$ ) enhancement both in: b) out-of-plane (OoP) and c) in-plane (IP) directions after annealing. d,e) The resulting magnetic face-centered tetragonal (fct)  $L1_0$  FePt nanopropellers exhibit higher magnetic coercivity (d) and remanent magnetization (e) than comparable Fe- or Ni-based nanopropellers.



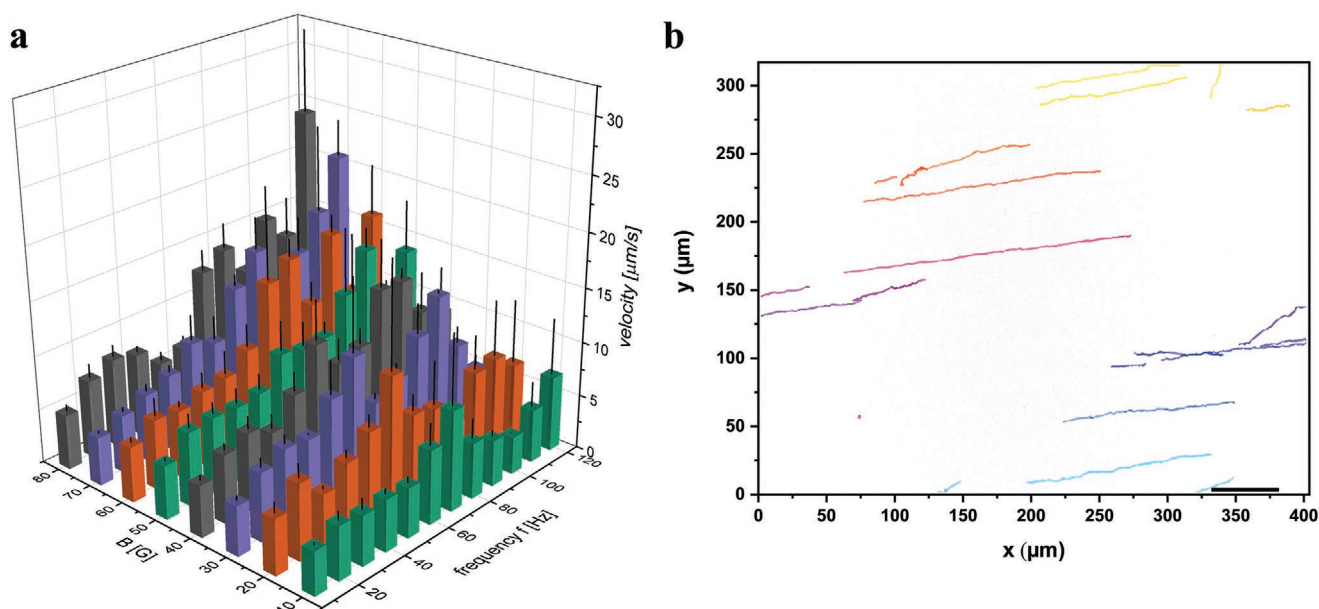


**Figure 3.** a) Mean propulsion velocities (at 1–8 mT, determined for at least 10 propellers) of magnetically propelled nanomotors (MPNs) increase as a function of magnetic field strength  $B$  rotation frequency unless they exhibit a step-out frequency. For clarity, graph shows mean propulsion between the 20th and 80th percentile to remove outliers. b) Trajectories obtained from a tracking video (Video S1, Supporting Information): MPN actuated at 3 mT and 80 Hz follow the predefined path. The trajectory colors are automatically assigned as a function of the tracks'  $y$ -position. Image colors are inverted for clarity. Scale bar is 50  $\mu\text{m}$ .

applications, despite a lower crystallinity and a slightly lower out-of-plane magnetization (along the long axis of the nanopropellers; Tables S1 and S2, Supporting Information). As mentioned above, the propellers have to be magnetized perpendicularly to the long axis of the nanomotor, thus a higher in-plane remanence is favorable.

The magnetic properties of the material used for the magnetic section or magnetic coating determine the maximum achievable torque,  $\tau$ , where  $\vec{\tau} = \vec{m} \times \vec{B}$ , where  $\vec{m}$  is the remanent magnetic moment and  $\vec{B}$  is the magnetic field vector. Lower fields can be used to obtain the same torque if the magnetic moment is higher, which simplifies the experimental setup and might thus eventually facilitate the implementation for clinical applications.

To examine the maneuverability and propulsion of the FePt propellers, a wafer of annealed, in-plane magnetized propellers is fluorescently labeled, submerged in deionized water, and sonicated to lift the particles off the wafer and transfer them to a solution. Particles are then subjected to rotating magnetic fields between 1 and 8 mT inside a 3-axis Helmholtz coil placed in a microscope. The magnetic nanopropellers are rotated with frequencies between 10 and 120 Hz and the propulsion speeds are tracked (Figure 3a). With the exception of nanomotors driven at 7 and 8 mT, a drop in propulsion speed (at the step-out-frequency) is observed for frequencies over 70 Hz. The propellers thus follow the commonly observed propulsion behavior.<sup>[26,60]</sup>

However, FePt nanopropellers, due to their higher magnetic moments, outperform magnetic propellers grown from Fe or Ni in terms of propulsion velocities.<sup>[18]</sup> The FePt structures could be propelled with fields as small as 1 mT in water (Videos S1 and S2, Supporting Information) and cell media (Video S3, Supporting Information) and exhibit mean velocities of up to

24  $\mu\text{m s}^{-1}$ , the equivalent of 13 body lengths  $\text{s}^{-1}$  (Figure 3a). Figure 3b shows exemplary parallel trajectories of several nanopropellers at 3 mT and 80 Hz. In previous work, we have already shown that we can also move a swarm of many thousand nanopropellers through the vitreous of the eye.<sup>[18]</sup>

As a final requirement for biomedical applications of magnetic nanodevices, the magnetic material should not cause any adverse or toxic effects. FePt and silica are the main components in the propellers and have both independently been subjected to extensive testing and have been identified as promising biocompatible materials.<sup>[3–4,30,61]</sup> Figure 4 shows the results of our studies conducted with the FePt–silica nanopropellers, where this shape and combination of materials are tested and shown to be nontoxic. Cytotoxicity and oxidative stress of the propellers are investigated by high-content cell imaging using propidium iodide (PI) staining and CellROX Green reagent, respectively. Viability of both A549 (Figure 4a) and HEK cell lines (Figure S4a, Supporting Information) is unaffected by the presence of particles at a ratio of 50:1 even after 72 h of incubation. In addition, no significant levels of reactive oxygen species are detected (Figure 4b; Figure S4b, Supporting Information). The FePt–silica nanopropellers are a route toward hard-magnetic biocompatible nanomotors and microdevices for biomedical applications.

To enable transfection with GLAD-grown nanopropellers, we adapt a proven transfection procedure,<sup>[62]</sup> which in turn enables one of three transfection mechanisms: i) via cells grown on a wafer of propellers, ii) via propellers in the cell medium (passive transfection), and iii) propellers in the cell medium with magnetic steering (active transfection) as seen in Figure 5a. In brief, the helices while still on the wafer are coated with a poly-cationic polymer (poly-D-lysine (PDL) or

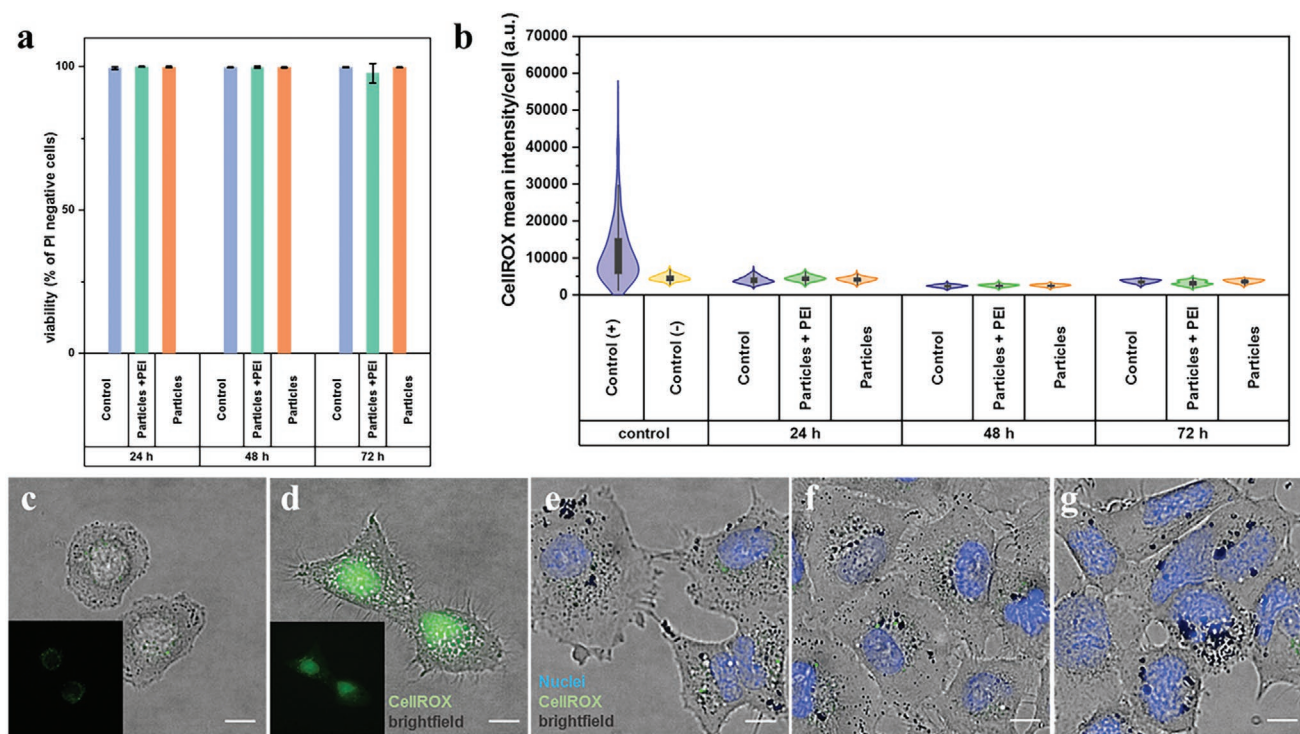


**Figure 4.** a) For incubation periods of up to 72 h, polyethyleneimine (PEI) coated and uncoated nanopropellers added to the cell media cause no adverse effects on the percentage of viable A549 cells, determined as negative for PI staining, even at concentrations as high as 50 propellers per cell. b) ROS production in A549 cells, incubated in the presence or the absence of PEI coated and uncoated particles, which is determined using CellROX green and quantified as mean fluorescence intensity per cell remains equally unaffected by the nanopropellers. c) Representative CellROX image of untreated A549 cells; d) positive control of cells treated with  $100 \times 10^{-6}$  M of menadione for 1 h at 37 °C shows bright green fluorescence while e–g) cells incubated with uncoated particles at a 50:1 ratio for 24 h (e), 48 h (f), or 72 h (g) do not. Scale bar is 10  $\mu$ m.

polyethyleneimine (PEI)) and an enhanced green fluorescent protein (EGFP) plasmid DNA as a reporter gene (Figure 1b). Next, A549 human alveolar epithelial cells are grown on top of the wafer and incubated for 24 h (Figure S5a, Supporting Information). After internalization of the helices, the cells express EGFP (Figure S5e–g, Supporting Information) whereas the control did not (Figure S5b–d, Supporting Information).

To evaluate the ability of dispersed magnetic nanopropellers to transfect adherent cells, nanopropellers are sonicated from the wafer and mixed into cell culture media at a final propeller to cell ratio of either 1:1 or 10:1. After 24 h, cells incubated with magnetic nanopropellers conjugated to EGFP plasmid expressed significantly more EGFP than control cells (Figure 5b), an effect that intensified after 72 h (Figure 5c). Our measure of determining significance is given in the “Statistical Analysis” section in the Supporting Information. Transfection exhibited a dose-dependent effect, as 10:1 propeller ratios produced a fourfold increase over 1:1 ratios in GFP signal compared to controls.

Finally, to enable active cell transfection, the magnetic structures have to be steerable toward specific target cells. Videos S3 and S4 in the Supporting Information and Figure 5e show a FePt nanopropeller navigating through the cell medium while being guided by the rotating magnetic field. The magnetic particle can be co-localized with the cell after the magnetic field is switched off and does not move further (Figure S6 and Videos S3 and S4, Supporting Information). A transfected cell expressing EGFP

after 24 h is pictured in Figure 5f. Adoption of the technology will require the independent control of multiple nanopropellers, that ideally are able to follow individual trajectories. This is a well-known and challenging task for magnetic micromotors. Some constructive first solutions have been proposed, such as exploiting multiple types of micromotors with slightly different material properties (i.e., step-out frequencies and magnetic moments).<sup>[60,63,64]</sup> While similarities exist with the transfection via plasmid-conjugated nanowires,<sup>[62]</sup> the latter is likely to involve cellular actomyosin contractility, which provides the force necessary for cellular nanowire “impalement.” In contrast, the use of nanopropellers does not require any contractile work from the target cells, and thus transfection is not dependent upon the ability of a given cell line to produce a traction force. This characteristic makes nanopropellers especially appealing in cells that have low levels of matrix adhesion and contractility, including embryonic stem cells, amoeboid cancer cells, and immune cells, as well as cells that are not rigidly attached.

In conclusion, we present a robust nanoscopic system suitable for navigation in vitro and gene delivery using nanometrically precise active magnetic carriers. These are grown using the L1<sub>0</sub> FePt which shows high magnetic remanence—rivaling the magnetic moments of NdFeB micromagnets. Our work thus establishes that complex-shaped micro- and nanostructures can be grown and processed such that they contain the hard magnetic biocompatible face-centered tetragonal L1<sub>0</sub> phase of FePt.

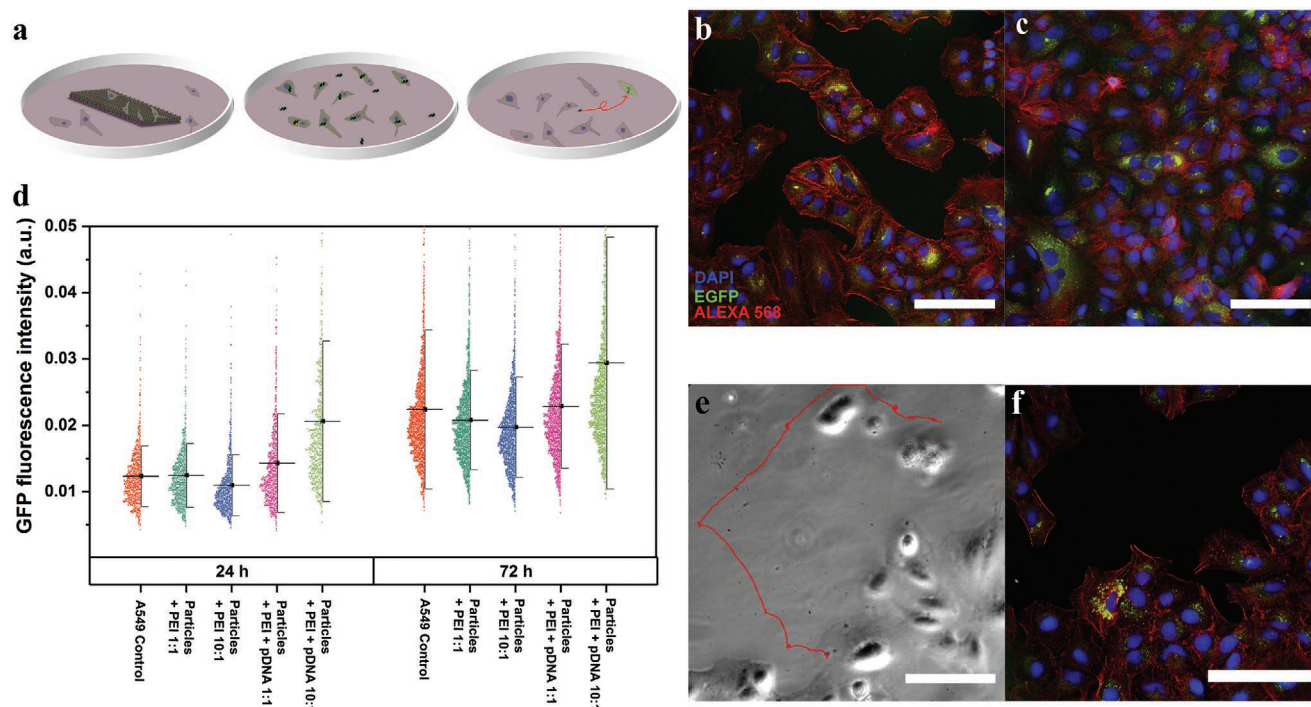


**Figure 5.** a) The illustration of three different conditions of cells in a Petri dish alongside PDL/PEI and EGFP plasmid coated nanopropellers depicts cells grown on top of a wafer, passive transfection, and active magnetic transfection from left to right. b,c) A549 cells incubated 1:1 with PEI-coated nanomotors for 24 h show green fluorescence (b), which intensifies after 72 h (c). d) Quantification of EGFP fluorescence intensity as a function of time equally shows a general increase from 24 to 72 h. Compared to the control as well as nonplasmid coated nanopropellers, both 1:1 and 10:1 ratios lead to an increase in EGFP fluorescence intensity. e) A PEI and EGFP plasmid coated nanopropeller follows a dictated path toward an A549 cell. f) Actively transfected A549 cell fluorescing green cell after 1 day of incubation. Cells are stained with Hoechst 33342 (blue channel) and ALEXA 568 Phalloidin (red channel). (b) and (c) are stained, mounted, and acquired on the same day with identical imaging settings. Scale bars are 100  $\mu\text{m}$ .

The magnetically driven nanopropellers could be moved with very small magnetic fields at velocities of up to 13 body lengths per second and navigated through cell media. In cell viability assays, the FePt swimmers are shown to be fully biocompatible with both A549 and HEK cell lines. The nanopropellers could be accurately steered toward specific cells, where transfection and gene delivery is achieved with polyethyleneimine-functionalized propellers. This study shows that FePt can be incorporated in micro- and nanodevices and presents an attractive system that should be further investigated for next-generation active magnetically driven probes for gene and drug delivery. Future work will explore the use of FePt swimmers as multimodal therapeutic and diagnostic agents combining MRI contrast agents with delivery. The growth and in situ processing of hard-magnetic FePt demonstrated herein opens the possibility to develop hard-magnetic biocompatible nanomotors and microdevices for biomedical applications.

## Experimental Section

**Fabrication of In-Plane Magnetized FePt Propellers:** GLAD had been described in detail in previous publications.<sup>[12,49,65,66]</sup> In brief, a monolayer of allyltrimethoxysilane-coated (Sigma-Aldrich) 500 nm silica beads was deposited on a 2 in. (51 mm) Si(100) wafer via Langmuir–Blodgett deposition.<sup>[65]</sup> The wafer was loaded into a physical vapor deposition chamber with a motorized stage (Figure 1a). Onto the rotating substrate, silica was then deposited at a glancing angle of 85°

via electron beam evaporation. After silica deposition, a 10 nm titanium adhesion layer was deposited followed by a co-deposition of 500 nm of Fe and Pt (1:1). The wafer was sealed inside a quartz vacuum tube and annealed at 300, 680, or 800 °C in a furnace for 1 h. The tubes were quenched in an ice bath and magnetized in-plane via SQUID magnetometry with an external field of 5 T.

**Functionalization with Poly-D-lysine and EGFP Plasmid:** 2 mL 0.1% poly-D-lysine (Gibco) was added to a dry 25 mm<sup>2</sup> wafer and incubated with the wafer for 4 h at 4 °C. The solvent was aspirated, the wafer washed with PBS, and gWiz EGFP plasmid DNA (Aldevron) was added and incubated overnight at 4 °C. Again, the solvent was aspirated, the wafer washed with PBS, and the nanomotors were lifted off in a sonication bath as described previously.<sup>[18,19]</sup>

**Functionalization with Polyethyleneimine and EGFP Plasmid:** 0.5 mL polyethyleneimine (25 kDa, branched, Sigma-Aldrich) was stirred in 30 mL of dry methanol. 0.11 mL 3-glycidooxy trimethoxypropyl silane (Sigma-Aldrich) was added after 30 min and the stir bar was removed. A dry 25 mm<sup>2</sup> wafer of nanopropellers was plasma cleaned prior to functionalization and was added to the solution and incubated overnight. The wafer was thoroughly washed with ethanol twice and twice with water. The solvent was aspirated, 2 mL water was added along with 100  $\mu\text{L}$  EGFP gWiz High Expression Reporter DNA (Aldevron), and was incubated overnight at 4 °C. Again, the solvent was aspirated, the wafer washed with PBS, and the nanomotors were lifted off in a sonication bath.

**A549 Cell Culture:** A549 lung carcinoma cells (ATCC) were cultured in F12K media (ATCC) supplemented with 10% fetal bovine serum inside T-75 cell culture flasks. Media was changed every 3 days, and cells were passaged at a ratio of 1:5 twice per week. Briefly, cell media was aspirated and replaced with 5 mL 0.25% trypsin-EDTA and incubated for 5 min at 37 °C, followed by trypsin deactivation in 5 mL of growth media.



**Nonmagnetic Transfection and Active Cell Transfection:** A549 were plated on a 35 mm glass-bottom Petri dish. A dispersion of functionalized propellers was diluted 1:10 with cell media (propeller media). After attachment of the cells, the media was aspirated and replaced by media containing propellers. For nonmagnetic transfection, the cells were then incubated for 24 h and subsequently fixed with 3.7% paraformaldehyde and mounted with Fluoromount G. For guided transfection, the glass bottom Petri dishes were transferred to a 3-axis Helmholtz coil inside a Zeiss AxioVert inverted microscope and the propellers were guided toward the cells using 2 mT rotating fields at 80 Hz.

**Confocal Microscopy and Analysis:** Fixed and stained cells were imaged on a Zeiss LSM 900 confocal microscope. Briefly, a 10-image array was collected from each well with the aid of 4',6-diamidino-2-phenylindole (DAPI) channel-based autofocus at each position. Resulting images were analyzed using an automated image analysis pipeline in CellProfiler (68).<sup>[67]</sup> Nuclear outlines were obtained as primary objects with manual thresholding from DAPI channel images, and cell outlines were obtained as secondary objects using a Watershed Gradient algorithm using the phalloidin channel. The pipeline calculated the mean and integrated density of the EGFP channel signal in nuclei and cell outlines. Data analysis was performed with Microsoft Excel and GraphPad Prism.

## Supporting Information

Supporting Information is available from the Wiley Online Library or from the author.

## Acknowledgements

The authors thank Cornelia Miksch, Athanasios Athanassiadis, Rahul Goyal, Mariana Alarcón Correa, and Samir Hammoud. This work was funded in part by the Vector Stiftung, Germany (Project 2018-0068). This work was supported by the Francis Crick Institute (to MGG), which receives its core funding from Cancer Research UK (FC001092), the UK Medical Research Council (FC001092), and the Wellcome Trust (FC001092).

## Conflict of Interest

The authors declare no conflict of interest.

## Keywords

biocompatible magnetic materials, FePt, gene delivery, iron platinum, magnetic nanopropellers, nano- and micromotors

Received: February 17, 2020

Revised: March 23, 2020

Published online:

- [1] C. S. Kumar, *Nanomaterials for Medical Diagnosis and Therapy*, John Wiley & Sons, Hoboken, NJ, USA **2007**.
- [2] S. Soares, J. Sousa, A. Pais, C. Vitorino, *Front. Chem.* **2018**, *6*, 360.
- [3] S.-W. Chou, Y.-H. Shau, P.-C. Wu, Y.-S. Yang, D.-B. Shieh, C.-C. Chen, *J. Am. Chem. Soc.* **2010**, *132*, 13270.
- [4] Y. Shi, M. Lin, X. Jiang, S. Liang, *J. Nanomater.* **2015**, *2015*, 13.
- [5] X. Xu, S. Hou, N. Wattanatorn, F. Wang, Q. Yang, C. Zhao, X. Yu, H.-R. Tseng, S. J. Jonas, P. S. Weiss, *ACS Nano* **2018**, *12*, 4503.

- [6] S. Chen, L. Wang, S. L. Duce, S. Brown, S. Lee, A. Melzer, S. A. Cuschieri, P. André, *J. Am. Chem. Soc.* **2010**, *132*, 15022.
- [7] L. K. E. A. Abdelmohsen, F. Peng, Y. Tu, D. A. Wilson, *J. Mater. Chem. B* **2014**, *2*, 2395.
- [8] L. Liu, J. Gao, D. A. Wilson, Y. Tu, F. Peng, *Chem. - Asian J.* **2019**, *14*, 2325.
- [9] W. Gao, J. Wang, *Nanoscale* **2014**, *6*, 10486.
- [10] S. Sánchez, L. Soler, J. Katuri, *Angew. Chem., Int. Ed.* **2015**, *54*, 1414.
- [11] J. Li, B. Esteban-Fernández de Ávila, W. Gao, L. Zhang, J. Wang, *Sci. Rob.* **2017**, *2*, eaam6431.
- [12] A. Ghosh, P. Fischer, *Nano Lett.* **2009**, *9*, 2243.
- [13] L. Zhang, J. J. Abbott, L. Dong, B. E. Kratochvil, D. Bell, B. J. Nelson, *Appl. Phys. Lett.* **2009**, *94*, 064107.
- [14] D. Xu, Y. Wang, C. Liang, Y. You, S. Sanchez, X. Ma, *Small* **2019**, *0*, 1902464.
- [15] B. Esteban-Fernández de Ávila, A. Martín, F. Soto, M. A. Lopez-Ramirez, S. Campuzano, G. M. Vázquez-Machado, W. Gao, L. Zhang, J. Wang, *ACS Nano* **2015**, *9*, 6756.
- [16] C. M. Maier, M. A. Huergo, S. Milosevic, C. Pernpeintner, M. Li, D. P. Singh, D. Walker, P. Fischer, J. Feldmann, T. Lohmüller, *Nano Lett.* **2018**, *18*, 7935.
- [17] L. Zhang, K. E. Peyer, B. J. Nelson, *Lab Chip* **2010**, *10*, 2203.
- [18] Z. Wu, J. Troll, H.-H. Jeong, Q. Wei, M. Stang, F. Ziemssen, Z. Wang, M. Dong, S. Schnichels, T. Qiu, P. Fischer, *Sci. Adv.* **2018**, *4*, eaat4388.
- [19] D. Walker, B. T. Käschorf, H.-H. Jeong, O. Lieleg, P. Fischer, *Sci. Adv.* **2015**, *1*, e1500501.
- [20] P. L. Venugopalan, R. Sai, Y. Chandorkar, B. Basu, S. Shivashankar, A. Ghosh, *Nano Lett.* **2014**, *14*, 1968.
- [21] W. Gao, R. Dong, S. Thamphiwatana, J. Li, W. Gao, L. Zhang, J. Wang, *ACS Nano* **2015**, *9*, 117.
- [22] B. E.-F. de Ávila, P. Angsantikul, J. Li, M. Angel Lopez-Ramirez, D. E. Ramirez-Herrera, S. Thamphiwatana, C. Chen, J. Delezuk, R. Samakapiruk, V. Ramez, M. Obonyo, L. Zhang, J. Wang, *Nat. Commun.* **2017**, *8*, 272.
- [23] X. Wei, M. Beltrán-Gastélum, E. Karshalev, B. Esteban-Fernández de Ávila, J. Zhou, D. Ran, P. Angsantikul, R. H. Fang, J. Wang, L. Zhang, *Nano Lett.* **2019**, *19*, 1914.
- [24] L. Kong, N. F. Rosli, H. L. Chia, J. Guan, M. Pumera, *Bull. Chem. Soc. Jpn.* **2019**, *92*, 1754.
- [25] D. Schamel, A. G. Mark, J. G. Gibbs, C. Miksch, K. I. Morozov, A. M. Leshansky, P. Fischer, *ACS Nano* **2014**, *8*, 8794.
- [26] A. Ghosh, D. Paria, H. J. Singh, P. L. Venugopalan, A. Ghosh, *Phys. Rev. E* **2012**, *86*, 031401.
- [27] R. Mhanna, F. Qiu, L. Zhang, Y. Ding, K. Sugihara, M. Zenobi-Wong, B. J. Nelson, *Small* **2014**, *10*, 1953.
- [28] F. Qiu, S. Fujita, R. Mhanna, L. Zhang, B. R. Simona, B. J. Nelson, *Adv. Funct. Mater.* **2015**, *25*, 1666.
- [29] H. Xu, M. Medina-Sánchez, V. Magdanz, L. Schwarz, F. Hebenstreit, O. G. Schmidt, *ACS Nano* **2018**, *12*, 327.
- [30] M. Pal, N. Somalwar, A. Singh, R. Bhat, S. M. Eswarappa, D. K. Saini, A. Ghosh, *Adv. Mater.* **2018**, *30*, 1800429.
- [31] M. Pal, D. Dasgupta, N. Somalwar, V. Reshma, M. Tiwari, D. Pally, S. M. Narayana, A. Katke, R. Jayashree, R. Bhat, *J. Phys.: Condens. Matter* **2020**, *32*, 224001.
- [32] M. Ermolli, C. Menné, G. Pozzi, M.-Á. Serra, L. A. Clerici, *Toxicology* **2001**, *159*, 23.
- [33] D. Guo, C. Wu, X. Li, H. Jiang, X. Wang, B. Chen, *J. Nanosci. Nanotechnol.* **2008**, *8*, 5316.
- [34] X. Lü, X. Bao, Y. Huang, Y. Qu, H. Lu, Z. Lu, *Biomaterials* **2009**, *30*, 141.
- [35] M. Ahamed, *Toxicol. In Vitro* **2011**, *25*, 930.
- [36] R. Karmhag, G. A. Niklasson, M. Nygren, *J. Appl. Phys.* **2001**, *89*, 3012.
- [37] W. H. Griffith, P. L. Pavcek, D. J. Mulford, *J. Nutr.* **1942**, *23*, 603.
- [38] R. Magaye, J. Zhao, L. Bowman, M. Ding, *Exp. Ther. Med.* **2012**, *4*, 551.



- [39] A. Cabot, V. F. Puentes, E. Shevchenko, Y. Yin, L. Balcells, M. A. Marcus, S. M. Hughes, A. P. Alivisatos, *J. Am. Chem. Soc.* **2007**, 129, 10358.
- [40] E. A. Gulbransen, T. P. Copan, *Nature* **1960**, 186, 959.
- [41] Y.-P. Sun, X.-q. Li, J. Cao, W.-x. Zhang, H. P. Wang, *Adv. Colloid Interface Sci.* **2006**, 120, 47.
- [42] Y. Fu, J. Chen, H. Zhang, *Chem. Phys. Lett.* **2001**, 350, 491.
- [43] B. Zhao, Y. Wang, H. Guo, J. Wang, Y. He, Z. Jiao, M. Wu, *Mater. Sci.-Pol.* **2007**, 25, 1143.
- [44] P. L. Venugopalan, S. Jain, S. Shivashankar, A. Ghosh, *Nanoscale* **2018**, 10, 2327.
- [45] X. Yan, Q. Zhou, J. Yu, T. Xu, Y. Deng, T. Tang, Q. Feng, L. Bian, Y. Zhang, A. Ferreira, L. Zhang, *Adv. Funct. Mater.* **2015**, 25, 5333.
- [46] H. Ceylan, I. C. Yasa, O. Yasa, A. F. Tabak, J. Giltinan, M. Sitti, *ACS Nano* **2019**, 13, 3353.
- [47] C. Peters, M. Hoop, S. Pané, B. J. Nelson, C. Hierold, *Adv. Mater.* **2016**, 28, 533.
- [48] K. Son, G. Ryu, H.-H. Jeong, L. Fink, M. Merz, P. Nagel, S. Schuppler, G. Richter, E. Goering, G. Schütz, *Small* **2019**, 15, 1902353.
- [49] K. Robbie, M. J. Brett, *J. Vac. Sci. Technol., A* **1997**, 15, 1460.
- [50] O. Yildirim, T. Gang, S. Kinge, D. N. Reinhoudt, D. H. Blank, W. G. van der Wiel, G. Rijnders, J. Huskens, *Int. J. Mol. Sci.* **2010**, 11, 1162.
- [51] K. Persson, *LBNL Materials Project*, Lawrence Berkeley National Lab. (LBNL), Berkeley, CA, USA **2016**.
- [52] C. F. Macrae, P. R. Edgington, P. McCabe, E. Pidcock, G. P. Shields, R. Taylor, M. Towler, J. van de Streek, *J. Appl. Crystallogr.* **2006**, 39, 453.
- [53] W. Hardaker, N. Schoeni, G. Chapuis, N. Casademont, M. Sisto, *Crystallography Applets and Simulation*, <http://escher.epfl.ch/recipeOgraph> (accessed: April 2020).
- [54] K. Elkins, D. Li, N. Poudyal, V. Nandwana, Z. Jin, K. Chen, J. P. Liu, *J. Phys. D: Appl. Phys.* **2005**, 38, 2306.
- [55] L. Suber, G. Marchegiani, E. S. Olivetti, F. Celegato, M. Coisson, P. Tiberto, P. Allia, G. Barrera, L. Piloni, L. Barba, F. Padella, P. Cossari, A. Chiolerio, *Mater. Chem. Phys.* **2014**, 144, 186.
- [56] N. Kikuchi, S. Okamoto, O. Kitakami, *J. Appl. Phys.* **2008**, 103, 07D511.
- [57] D. Harimoto, Y. Matsura, *Tech. Rev.* **2007**, 23, 69.
- [58] K. P. Su, Z. W. Liu, D. C. Zeng, D. X. Huo, L. W. Li, G. Q. Zhang, *J. Phys. D: Appl. Phys.* **2013**, 46, 245003.
- [59] P. Cavallotti, B. Bozzini, R. Cecchini, G. F. Bava, H. A. Davies, C. Hoggarth, *J. Magn. Magn. Mater.* **1992**, 104–107, 1216.
- [60] P. Katsamba, E. Lauga, *Phys. Rev. Appl.* **2016**, 5, 064019.
- [61] H. Jaganathan, B. Godin, *Adv. Drug Delivery Rev.* **2012**, 64, 1800.
- [62] R. Elnathan, B. Delalat, D. Brodoceanu, H. Alhmoud, F. J. Harding, K. Buehler, A. Nelson, L. Isa, T. Kraus, N. H. Voelcker, *Adv. Funct. Mater.* **2015**, 25, 7215.
- [63] P. Mandal, V. Chopra, A. Ghosh, *ACS Nano* **2015**, 9, 4717.
- [64] U. K. Cheang, K. Lee, A. A. Julius, M. J. Kim, *Appl. Phys. Lett.* **2014**, 105, 083705.
- [65] D. Schamel, M. Pfeifer, J. G. Gibbs, B. Miksch, A. G. Mark, P. Fischer, *J. Am. Chem. Soc.* **2013**, 135, 12353.
- [66] A. G. Mark, J. G. Gibbs, T.-C. Lee, P. Fischer, *Nat. Mater.* **2013**, 12, 802.
- [67] L. Kametsky, T. R. Jones, A. Fraser, M. A. Bray, D. J. Logan, K. L. Madden, V. Ljosa, C. Rueden, K. W. Eliceiri, A. E. Carpenter, *Bioinformatics* **2011**, 27, 1179.